nature astronomy

SUPPLEMENTARY INFORMATION

https://doi.org/10.1038/s41550-019-0779-y

In the format provided by the authors and unedited.

Molybdenum isotopic evidence for the late accretion of outer Solar System material to Earth

Gerrit Budde*, Christoph Burkhardt and Thorsten Kleine

Institut für Planetologie, University of Münster, Wilhelm-Klemm-Straße 10, 48149 Münster, Germany. *e-mail: gerrit.budde@uni-muenster.de

Supplementary Information

Molybdenum isotopic evidence for the late accretion of outer Solar System material to Earth

G. Budde, C. Burkhardt, T. Kleine

This file includes:
Supplementary Methods and Discussion
Supplementary Figures 1–6
Supplementary Tables 1–4

S1 Mo isotope data

The Mo concentration and isotope data obtained for terrestrial samples, bulk meteorites, and acid leachates are provided in Supplementary Table 1. Molybdenum concentrations of the analysed bulk meteorites typically range between ~0.2 and ~2 ppm. The amounts of Mo released in the various leachate steps of the unequilibrated ordinary chondrites (UOC) are highly variable (Supplementary Fig. 3). While the least Mo is released in the L1 and L6 steps, the largest fraction of Mo is released in the L2 (NWA 2458) or L5 (WSG 95300) steps. For NWA 2458 the total amount of Mo released (~3960 ng) in the leaching steps is consistent with the amount expected from the whole rock analyses (*i.e.*, >90% of the expected Mo was released during the leaching procedure).

All meteorite samples investigated here display well-resolved Mo isotope anomalies relative to the bracketing standard ($\varepsilon^{i}Mo \equiv 0$), the magnitude of which decrease in the order $\varepsilon^{92}Mo > \varepsilon^{94}Mo > \varepsilon^{95}Mo > \varepsilon^{100}Mo > \varepsilon^{97}Mo$. Independent of the magnitude of the anomalies, all samples exhibit the typical *w*- or *m*-shaped Mo isotope patterns that are indicative of a deficit or excess, respectively, in *s*-process Mo nuclides (*e.g.*, ref. 37) (Supplementary Fig. 4). In diagrams of $\varepsilon^{i}Mo$ versus $\varepsilon^{i}Mo$ (*e.g.*, Supplementary Fig. 5; Fig. 1) all samples generally plot along mixing lines between terrestrial Mo and a presumed component depleted (or enriched) in *s*-process Mo as measured in mainstream SiC grains[19]. Therefore, the measured Mo isotope anomalies are nucleosynthetic in origin, predominantly reflecting the heterogeneous distribution of an *s*-process carrier.

The anomalies in the bulk meteorites range between $\varepsilon^{92}Mo \approx 0.5$ (RC, aubrites) and $\varepsilon^{92}Mo \approx 2.3$ (CK, CH, Tafassasset), and samples from a given meteorite group typically have indistinguishable Mo isotope anomalies; the only exception are ureilites, which show some

resolved variability. While most ureilite samples cluster around an ε^{92}Mo of ~1 and mostly overlap within uncertainty, two monomict ureilites (EET 87517, PCA 82506) are characterized by significantly larger ε^{i}Mo excesses. These two samples were thus not included in the ureilite average (Supplementary Table 1) and plotted as individual points in Fig. 1. The nucleosynthetic isotope variability among ureilites likely results from the separation of isotopically distinct phases during partial differentiation of the ureilite parent body, as previously observed for Os isotopes[38]. As such, it remains unclear as to whether the calculated average is representative for the original bulk Mo isotopic composition of the ureilite parent body. However, all individual ureilites plot on the NC-line as defined below (Section S2), and so the observed variability among them is caused by variable deficits in *s*-process Mo nuclides. Thus, even if the bulk Mo isotopic composition of the original ureilite parent body was different from that measured for ureilites themselves, it would still plot on the NC-line.

Compared to bulk meteorites, the ordinary chondrite leachates display a much larger range of anomalies with ε^{92}Mo values between about –25 and +8. Consistent with the disparate Mo release patterns, the UOC samples also show very different Mo isotope compositions for the respective leachate steps (Supplementary Fig. 3). NWA 2458 is characterized by an overall trend from positive ε^{i}Mo values in the initial leachates to negative ε^{i}Mo values in the last leachate steps. In contrast, for WSG 95300 the Mo isotope anomalies appear arbitrarily distributed among the different leaching steps. For instance, the L3 step shows the largest *s*-process excess, whereas the L6 step displays the largest *s*-process deficit. The origin of the disparate isotope systematics in the L and H chondrite leachates is unclear at this point, but is probably is related to the redistribution of presolar components during nebular or parent-body processes. Nevertheless, the leachates plot on single well-defined correlation lines in ε^{i}Mo–ε^{i}Mo diagrams and, therefore, allow for the precise determination of the slopes of these lines (Supplementary Fig. 5). Only the leachate step L6 from WSG 95300 stands out by deviating from these correlation lines and is thus excluded from further discussion. Note, however, that including this leachate would yield identical results, albeit with larger uncertainties, for the NC-line regression (Section S2).

In a diagram of ε^{95}Mo versus ε^{94}Mo, in which the difference between *s*- and *r*-process variations is most pronounced, the analysed carbonaceous chondrites (CK, CH, CB) and Tafassasset plot on a distinct *s*-process mixing line than the other meteorites (Fig. 1). This observation is consistent with previous studies[11-15], which demonstrated that carbonaceous (CC) meteorites are characterized by a positive offset relative to non-carbonaceous (NC) meteorites in the ε^{95}Mo–ε^{94}Mo diagram, which most likely reflects an approximately constant *r*-process excess[12] or, alternatively, coupled *r*- and *p*-process excesses[14] in CC over NC materials. In contrast, all other bulk meteorites and the acid leachates analysed in the present study plot on a correlation line with enstatite and ordinary chondrites as well as most iron meteorites and other achondrites (see Section S2 for definition of NC-line), demonstrating that all these samples (*i.e.*, Rumuruti chondrites, acapulcoites, angrites, aubrites, brachinites, mesosiderites, ureilites, and the ungrouped achondrite NWA 1058) belong to the NC group of meteorites. Therefore, the new data presented here confirm and extend the fundamental dichotomy between CC and NC materials observed in previous studies to a much larger range of meteorite groups. So far, the Mo isotope dichotomy holds for all analysed samples (more than 40 meteorite groups and ungrouped meteorites; Supplementary Table 4), where the fact that all meteorites plot on either the CC- or the NC-line (and not in between) supports an efficient separation of two genetically distinct source regions of planetesimals.

S2 Calculation of CC- and NC-lines

The Mo isotopic data from this study, combined with previously reported results, allow a more precise calculation of the slopes and intercepts of the NC- and CC-lines. All regressions were calculated using the 'Model 1 fit' of *Isoplot* (v3.76), which is a York regression weighting the data points proportional to the inverse square of their assigned errors, where the reported uncertainties represent 95% confidence intervals (95% CI). The CC-line (Carbonaceous Chondrite-line) has already been precisely defined in prior studies using different kinds of sub-samples from carbonaceous chondrites (such as acid leachates and component-specific separates), all of which plot on the CC-line and, thus, have the same *r*-excess that is characteristics for CC materials in general[12,36]. For consistency, however, the CC-line was also recalculated using the same regression method, and including the new data for carbonaceous meteorites from this study.

A summary of all the bulk meteorite data used for the regressions, including data from this and previous studies, is provided in Supplementary Table 4. Note that the Mo isotopic composition of iron meteorites may have been modified owing to interaction with galactic cosmic rays (GCR)[11,15]. For the definition of the NC- and CC-lines we, therefore, only used data for iron meteorites for which such effects were corrected or are negligible, as demonstrated by minor to absent GCR effects on Pt and Os isotopes.

Some prior studies have argued that the nucleosynthetic isotope composition of primitive chondrites may not reflect that of the original bulk body, because alteration on the parent body may have mobilized and redistributed isotopically anomalous Mo from presolar phases[11,39]. In addition, owing to the presence of isotopically anomalous components, primitive chondrites may be isotopically heterogeneous at the sampling scale. These issues likely do not exist with iron meteorites because they formed by large-scale melting and metal segregation, which led to complete homogenization of presolar phases prior to metal-silicate fractionation. As noted above, however, among the differentiated meteorites, the isotopic composition of ureilites may not be representative for that of the bulk parent body. Nevertheless, all analysed bulk meteorites plot along either the NC- or the CC-line, indicating that the isotopic variations within each group predominantly reflect *s*-process variations. Thus, any unrepresentative sampling of bulk parent body compositions, if it occurred, only resulted in variations along either NC- or the CC-line, but not in significant deviations from either of the lines. Consequently, for the purpose of defining the slopes and intercepts of the NC- and CC-lines, possible deviations of chondrite compositions from their bulk parent body composition is inconsequential.

The CC-line can precisely be determined using the data for carbonaceous chondrites, including the new data for CK, CH, and CB chondrites from this study, and their components. This includes (*i*) chondrule and matrix separates from Allende (CV3)[12], (*ii*) metal, silicate, and chondrule separates from CR2 chondrites[36], (*iii*) acid leachates from Murchison (CM2), Allende (CV3), and Orgueil (CI1)[40,41], and (*iv*) bulk carbonaceous chondrites (CI, CM, CO, CV, CK, CR, CH, CB). A linear regression of this data set yields $\varepsilon^{95}Mo = (0.596\pm0.006) \times \varepsilon^{94}Mo + (0.26\pm0.02)$ [MSWD=1.3], consistent with the results in ref. 12. Several iron meteorites (IIC, IID, IIF, IIIF, IVB, and some ungrouped irons) and achondrites (*e.g.*, Eagle Station and Milton pallasites, Tafassasset) also plot on the CC-line; including these samples in the regression yields exactly the same result for the CC-line, but a slightly improved MSWD of 1.1.

The NC-line (Non-Carbonaceous-line) was previously defined as $\varepsilon^{95}Mo = (0.47\pm0.14) \times \varepsilon^{94}Mo - (0.02\pm0.10)$, based on data for enstatite and ordinary chondrites as well as some iron meteorites and achondrites[12]. The large uncertainties on both the slope and intercept reflect the limited range of Mo isotope anomalies among these samples, and also the poor precision

of some previous data. A linear regression including (*i*) the new data for bulk NC meteorites from this study (RC, achondrites) together with previously reported data (OC, EC, iron meteorites) and (*ii*) the data for the acid leachates from the ordinary chondrites, yields $\varepsilon^{95}Mo = (0.596\pm0.008) \times \varepsilon^{94}Mo - (0.09\pm0.02)$ [MSWD=1.2] (Supplementary Fig. 5). Bulk NC meteorites alone define a less precise correlation line with $\varepsilon^{95}Mo = (0.530\pm0.051) \times \varepsilon^{94}Mo - (0.06\pm0.04)$ [MSWD=0.52] with a slightly shallower slope. This slightly different slope suggests that the Mo isotope variations among the NC meteorites are not entirely governed by *s*-process heterogeneity, but that additional small *p*- and/or *r*-process heterogeneities may also exist. However, a regression of only the bulk NC meteorite data with a predefined slope of 0.596 results in an equally good fit (MSWD=0.78). This and the low MSWD of 1.2 for the combined regression (*i.e.*, including bulk meteorites and leachates) demonstrate that the Mo isotope variations among the NC meteorites almost entirely reflect *s*-process variations, and that any additional *p*- and/or *r*-process heterogeneities are minor to absent. The characteristic composition of the NC-line is, therefore, best defined by the combined regression of all data, including the leachates and bulk NC meteorites. Finally, we note that any possible *p*- and/or *r*-process heterogeneity among bulk NC meteorites is small compared to the offset between the NC- and CC-lines (Fig. 1), and is therefore inconsequential for the purpose of using the NC- and CC-lines for reconstructing Earth's accretion history.

With the new Mo isotope data obtained here, both the CC- and NC-lines are now precisely defined. Both lines have an identical slope of 0.596 (in $\varepsilon^{95}Mo$ versus $\varepsilon^{94}Mo$ space), which is in excellent agreement with a mixing line between terrestrial Mo and a presumed component depleted/enriched in *s*-process Mo as measured in mainstream SiC grains ($m \approx 0.59$)[19]. However, the CC- and NC-lines are characterized by significantly different *y*-axis intercepts. The fact that both lines are parallel makes it meaningful to calculate (analogously to the $\Delta^{17}O$ notation) a $\Delta^{95}Mo$ value for a given sample (see main text), which represents the vertical deviation (in parts-per-million) of a sample from a reference line with $\varepsilon^{95}Mo = 0.596 \times \varepsilon^{94}Mo$ (Supplementary Fig. 1). Note that the *y*-intercept of the CC- and NC-line regressions essentially define the $\Delta^{95}Mo$ values of 26±2 and –9±2 (95% CI) for the CC and NC reservoirs, respectively.

S3 Mo isotope composition of bulk silicate Earth

Constraining the relative contributions of NC and CC material to the Earth requires knowledge of the Mo isotope composition of the Earth's mantle. High purity elemental standards are not always good proxies for the mass-independent isotopic composition of the Earth's mantle[21,22], because isotope fractionation induced during production of the standards may not adequately be described by the exponential law, which is conventionally used for correction of instrumental mass fractionation in the isotope measurements. This may lead to small residual anomalies for internally-normalized isotope ratios. For example, several studies have shown that industrially produced steel standards (*e.g.*, NIST SRM 129c and 82b) are affected by mass-dependent Mo isotope fractionation that cannot be described by the exponential law, resulting in anomalous (lower) $\varepsilon^{i}Mo$ values relative to the solution standard[14,36,37] (Supplementary Fig. 6). This example highlights that the Mo isotope composition of the bulk silicate Earth (BSE) must be determined by the analyses of terrestrial rock samples.

We analysed a suite of terrestrial rock samples, including different lithologies such as basalts (BCR-2, BHVO-2, JB-2), andesites (JA-2), granodiorites (JG-1), diabases (W-2a), and

dunites (DTS-2b). These samples represent different mantle sources and have highly variable Mo concentrations as well as chemical compositions, and so potential effects of different sample matrices on measured Mo isotope compositions can be ruled out. Of these samples, the USGS reference materials BHVO-2 and, in particular, BCR-2 are heavily contaminated with Mo from steel tools used in the preparation of the sample powders[42]. Consistent with this, the Mo isotope compositions measured for BHVO-2 and BCR-2 slightly deviate from those obtained for the other rock samples, and are shifted towards the compositions measured for the steel standards (Supplementary Fig. 6). As such, BHVO-2 and BCR-2 were not used for the calculation of the BSE composition (Supplementary Table 1).

The other terrestrial rock standards investigated here (JB-2, JA-2, JG-1, W-2a, DTS-2b) have indistinguishable Mo isotope compositions, characterized by a small, albeit systematic, offset ($\varepsilon^{94}Mo = 0.04\pm0.06$; $\varepsilon^{95}Mo = 0.10\pm0.04$) from the composition of the Mo solution standard ($\varepsilon^{i}Mo \equiv 0$). A similar offset has also been observed for diamictites and OIBs in a Mo isotope study using thermal ionization mass spectrometry (TIMS)[11], demonstrating that this offset is present for both MC-ICP-MS and TIMS measurements. Therefore, the small offset from zero is not an artefact introduced by a particular measurement method, but is an inherent difference between terrestrial rock samples and the solution standards. As such, this difference most likely results from non-exponential isotopic fractionation (*i.e.*, fractionations that are not accounted for by the mass fractionation correction during the measurements) induced during purification and enrichment of Mo in the production of the solution standard, or during the genesis of the Mo ores from which these standards are produced. The latter would be consistent with the observation that molybdenites have Mo isotope compositions that are closer to those of the solution standards (Supplementary Fig. 6). As such, both the solution standards and the molybdenites do not provide good proxies for the Mo isotope composition of the BSE; this composition is instead best defined by the data for the terrestrial rock samples.

The BSE composition defined by the mean of the analysed rock samples from this study (Supplementary Table 1) is consistent with, albeit much more precise than the composition defined by ref. 11 ($\varepsilon^{94}Mo = 0.09\pm0.27$; $\varepsilon^{94}Mo = 0.08\pm0.15$), and plots between the CC- and NC-lines in a diagram of $\varepsilon^{95}Mo$ versus $\varepsilon^{94}Mo$ (Fig. 2). The $\Delta^{95}Mo$ value for the BSE, based on our data, is 7±5 (95% CI, n=5), which is clearly resolved from the values of CC and NC materials. Of note, all individual terrestrial samples analysed in this and previous studies, including steel samples, steel-contaminated rock standards, and solution standards, plot between the CC- and NC-lines. Including such samples in the calculation of the BSE's $\Delta^{95}Mo$ would result in a value of 5±4 (95% CI, n=10), which is indistinguishable from the value defined above. Thus, the particular choice of the exact samples used to define the BSE composition has no significant effect on the main conclusion that the Mo isotope composition of the present-day BSE is intermediate between those of the CC and NC materials.

The offset of the BSE's Mo isotopic composition from the NC-line cannot reflect any mass-dependent isotopic fractionation, neither among the analysed terrestrial samples nor between the BSE and Earth's core. All data are corrected for natural and instrumental mass-dependent isotope fractionation, and so the observed isotopic variations are mass-independent in nature. This is confirmed by comparing the isotopic data in diagrams of $\varepsilon^{95}Mo$ versus $\varepsilon^{94}Mo$ and $\varepsilon^{95}Mo$ versus $\varepsilon^{92}Mo$ (Supplementary Fig. 2). The former diagram is the classical diagram in which the NC-CC dichotomy is most clearly resolved. However, this dichotomy is also present in the latter diagram, although the difference between the NC- and CC-lines is smaller and analytical uncertainties on $\varepsilon^{92}Mo$ are typically larger. First, in the $\varepsilon^{95}Mo$–$\varepsilon^{94}Mo$ diagram, any mass-dependent isotope fractionation would follow a slope of ~0.5 [$(m^{95}Mo–m^{96}Mo)/(m^{94}Mo–m^{96}Mo)$], which is about the same as that of the NC-line (m=0.596); this process, therefore,

cannot cause a significant deviation of the BSE value from the NC-line. Second, in the ε^{95}Mo–ε^{92}Mo diagram, any mass-dependent isotope fractionation would follow a slope of ~0.25 [(m^{95}Mo–m^{96}Mo)/(m^{92}Mo–m^{96}Mo)], which is significantly shallower than that of the NC-line (m=0.483). Thus, in this diagram the position of the BSE could in principle be shifted away from the NC-line by unaccounted mass-dependent fractionation effects. However, in both the ε^{95}Mo–ε^{94}Mo and ε^{95}Mo–ε^{92}Mo diagrams, the BSE plots between the NC- and CC-lines and the relative distances between the BSE and the two lines are the same in both plots. Specifically, the mass fraction of CC-derived Mo (f_{CC}) in the BSE as calculated from the ε^{95}Mo–ε^{94}Mo systematics is 0.46±0.15, and the exact same number (0.46±0.34), albeit with larger uncertainty, is obtained from the ε^{95}Mo–ε^{92}Mo diagram. This consistency demonstrates that the Mo isotopic data are free of any unaccounted mass-dependent effects, because otherwise the ε^{95}Mo–ε^{94}Mo and ε^{95}Mo–ε^{92}Mo systematics would be significantly different. Finally, any mass-dependent Mo isotope fractionation induced during core formation would be very small and—although such a fractionation has been observed experimentally[43]—the temperature of core formation in the Earth was too high to lead to any resolvable mass-dependent Mo isotope fractionation between the BSE and the core[44].

S4 Predicted Δ^{95}Mo of bulk silicate Earth

The Mo present in the bulk silicate Earth (BSE) can be viewed as a mixture of three components: proto-Earth's mantle (*pE*), the giant Moon-forming impactor (*GI*), and the late veneer (*LV*). For the mass balance equations, the following parameters were used:

- g = impactor-to-Earth ratio (assumed to be 0.1; *i.e.*, a Mars-sized impactor[23]). For simplicity we assume that all of the impactor mass is accreted by Earth.
- k = mass fraction of the Moon-forming impactor core that equilibrated with Earth's mantle; note that this does not include the late veneer, which is the material added after the formation of the Moon and cessation of core formation.
- f = mass fraction of the late veneer. This value is obtained from absolute abundances of highly siderophile elements in the bulk silicate Earth, which provides a mass fraction of the late veneer of 0.7±0.2% of the mass of the Earth's mantle[24]. A higher mass fraction of the late veneer is possible if it is assumed that the late veneer consistent of differentiated lunar-sized projectiles, whose core partially merged with Earth's core without prior equilibration with Earth's mantle[45]. However, the Mo contained in the core material that did not equilibrate would not have contributed to the Mo in the present-day BSE. Thus, for estimating the effect of the late veneer on the BSE's Mo isotopic composition, the mass fraction inferred from the abundances of the highly siderophile elements is appropriate.
- γ = mantle mass fraction. A constant value of 0.675 was assumed for both Earth and the impactor.
- D = metal-silicate partition coefficient for Mo; this value varies from ~100 to ~1000 depending on various parameters, including pressure, temperature, and oxygen fugacity[46]. However, for the final core formation event in the Earth, which directly followed the giant impact, this value is more precisely defined from the Mo concentration in the BSE compared to that in chondrites, and a D_E value between 100 and 200 has been inferred[46]; here this value is assumed for the final core formation event in the Earth. For core formation in the impactor, the value for D_{GI} is essentially unknown and values between 100 and 1000 were assumed[46].

First, the Mo concentrations in the relevant reservoirs are calculated. The pre-late veneer Mo concentration of the bulk silicate Earth is

$$[Mo]_{pre-LV} = \frac{[Mo]_{BSE} - f[Mo]_{LV}}{1-f}$$

where the Mo concentration of the late veneer is assumed to be chondritic (*i.e.*, 900–1600 ppb[37,47]). For the BSE, a Mo concentration of 23±7 ppb is used[44], indicating that roughly 20–30% of the BSE's Mo derives from the late veneer. The Mo concentration of the giant impactor material that equilibrated with the Mo in the proto-Earth's mantle is

$$[Mo]_{GI} = \frac{\gamma + k(1-\gamma)D_{GI}}{\gamma + (1-\gamma)D_{GI}}[Mo]_{chondrites}$$

where D_{GI} is the metal-silicate partition coefficient appropriate for core formation in the Moon-forming impactor. The Mo concentration of the bulk impactor is assumed to be chondritic. The Mo concentration in proto-Earth's mantle then is

$$[Mo]_{pE} = \frac{[Mo]_{post-GI} - g[Mo]_{GI}}{1-g}$$

where $[Mo]_{post-GI}$ is the Mo concentration in the silicate Earth after addition of the giant impactor but before segregation of impactor core material to the Earth:

$$[Mo]_{post-GI} = \frac{\gamma + gk(1-g)D_E}{\gamma + gk(1-g)}[Mo]_{pre-LV}$$

The Δ^{95}Mo of the pre-late veneer silicate Earth is then given by

$$\Delta^{95}Mo_{pre-LV} = \frac{(1-g)[Mo]_{pE}\Delta^{95}Mo_{pE} + g[Mo]_{GI}\Delta^{95}Mo_{GI}}{[Mo]_{post-GI}}$$

and the final predicted Δ^{95}Mo of the BSE can be computed as follows:

$$\boldsymbol{\Delta^{95}Mo_{BSE}} = \frac{\boldsymbol{(1-f)[Mo]_{pre-LV}\Delta^{95}Mo_{pre-LV} + f[Mo]_{LV}\Delta^{95}Mo_{LV}}}{\boldsymbol{(1-f)[Mo]_{pre-LV} + f[Mo]_{LV}}}$$

With these governing equations the predicted Δ^{95}Mo of the BSE can be calculated for different assumed Δ^{95}Mo values of the giant impactor, proto-Earth's mantle and the late veneer. The uncertainties on all parameters were propagated by a Monte Carlo simulation, where all parameters were varied randomly within their given bounds as given above, and values for *k* were varied randomly between 0 (no equilibration) and 1 (full equilibration). The calculations were performed for several distinct sets of assumed compositions of the giant impactor, proto-Earth's mantle and the late veneer, including different combinations of pure CC (Δ^{95}Mo = +26±2), pure NC (Δ^{95}Mo = –9±2), and mixed NC-CC compositions. For simplicity, the mixed NC-CC compositions were assumed to be within the range of the observed Δ^{95}Mo

for the BSE (Δ^{95}Mo = +7±5). The results of the calculations are plotted in Fig. 3, where the dots in each panel represent the outcome of the Monte Carlo simulation with N≈30,000.

For each set of assumed compositions for the giant impactor, proto-Earth's mantle, and the late veneer, the results of the calculations are translated into probabilities to match the BSE's Δ^{95}Mo by comparing the number of solutions matching the BSE's Δ^{95}Mo of 7±5 to the total number of solutions. This comparison is done in steps of *k* of 0.02, so that for each step a probability is obtained. The resulting probabilities are plotted in Fig. 4 as a function of the degree of impactor core re-equilibration (*k*).

S5 Supplementary Figures and Tables

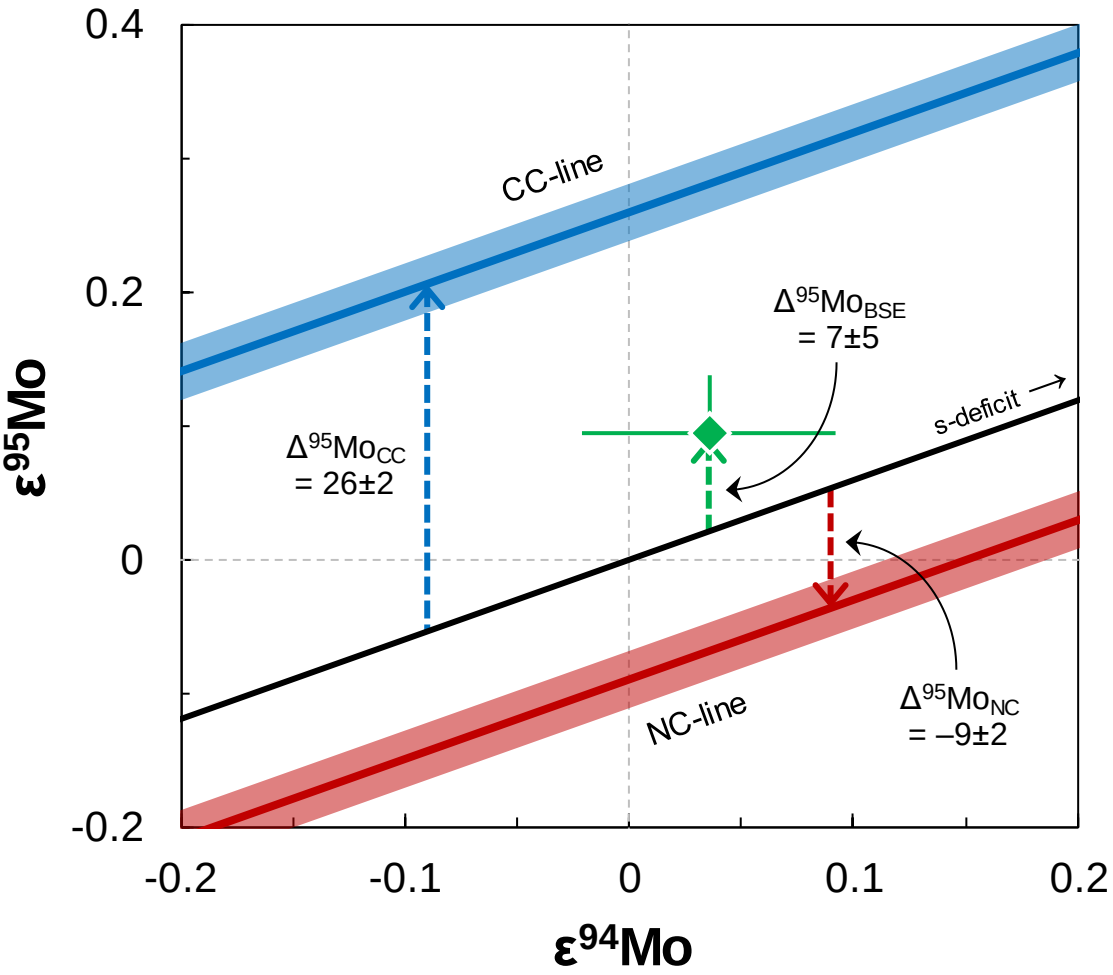

Supplementary Figure 1. Schematic diagram of ε^{95}Mo versus ε^{94}Mo. Solid black line is an *s*-process mixing line passing through zero (*i.e.*, the composition of the Mo standard). Δ^{95}Mo represents the vertical deviation (in parts-per-million) of a given sample from this reference line. Irrespective of the absolute isotope anomaly, CC and NC samples are characterized by distinct Δ^{95}Mo, while the BSE has an intermediate value. Error envelopes represent 95% confidence intervals (95% CI) of the CC- and NC-line regressions (see Section S2 for details).

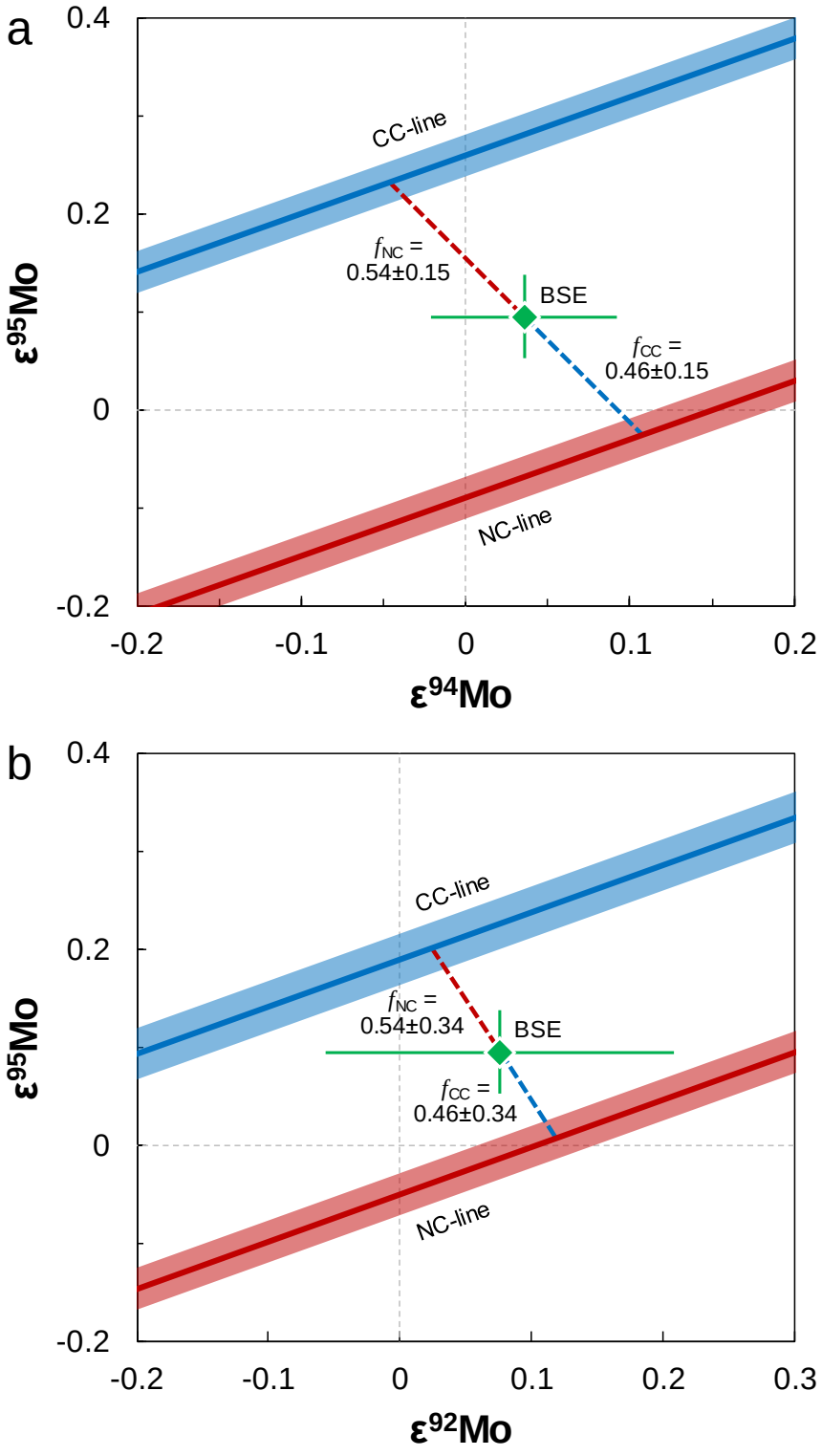

Supplementary Figure 2. Diagrams of ε^{95}Mo versus ε^{94}Mo (a) and ε^{92}Mo (b). In both diagrams, carbonaceous (CC, blue) and non-carbonaceous (NC, red) meteorites define two parallel lines. Hence, the BSE composition divides any tie line between the NC- and CC-lines into two segments whose ratio to each other is constant (examples shown here). This allows quantifying the relative contributions of NC and CC material regardless of the position of the endmembers on the lines, which are the same in both diagrams. Note that in the ε^{95}Mo–ε^{92}Mo diagram (b) the uncertainties are generally larger, and the CC- and NC-lines are ε^{95}Mo = (0.482±0.005) × ε^{92}Mo + (0.19±0.03) and ε^{95}Mo = (0.483±0.008) × ε^{92}Mo – (0.05±0.02), respectively (calculated as described in Section S2 for the ε^{95}Mo–ε^{94}Mo diagram).

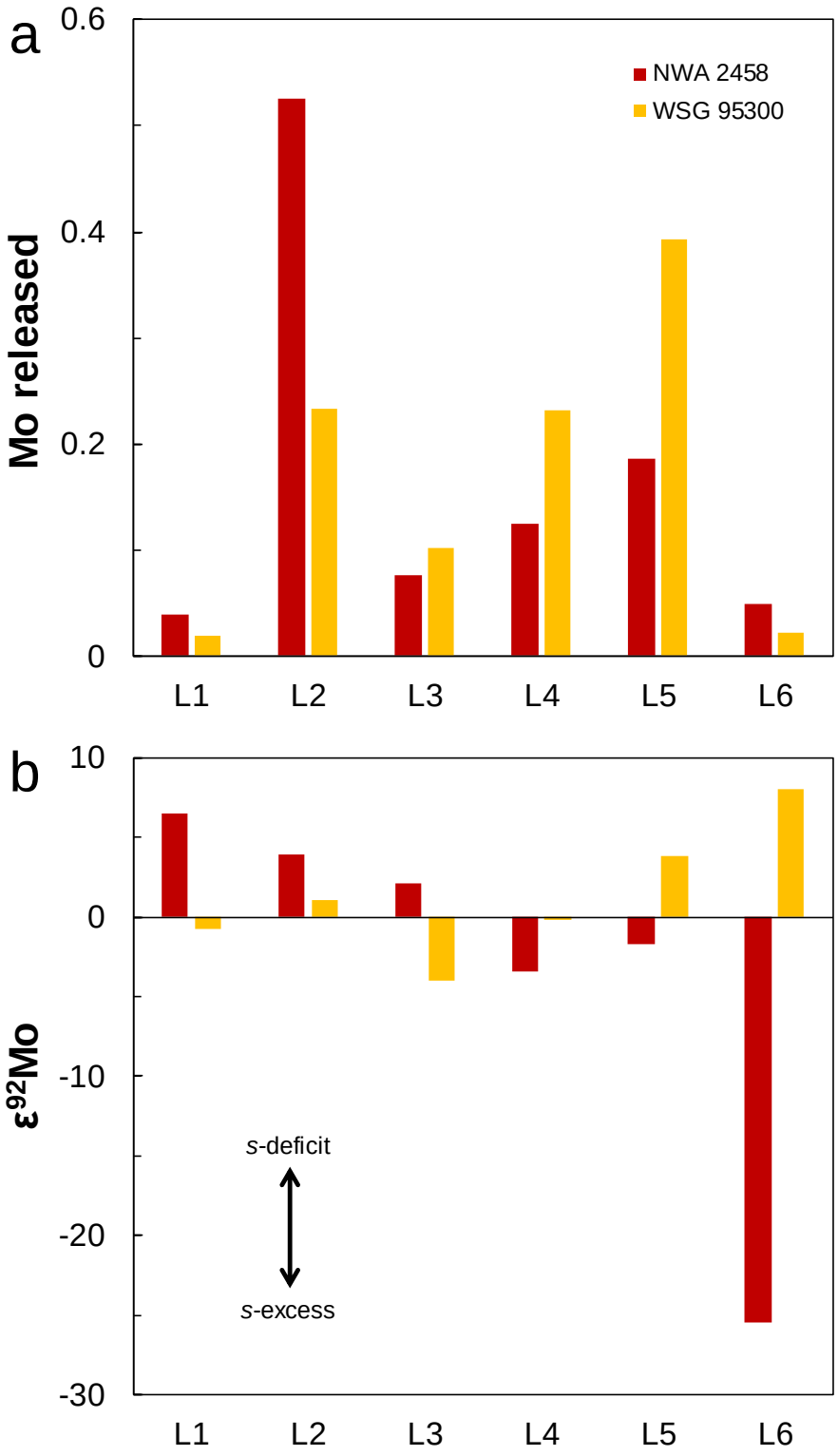

Supplementary Figure 3. Fraction of Mo released (a) and ε^{92}Mo (b) for the different leaching steps. The two unequilibrated ordinary chondrites NWA 2458 (L3.2) and WSG 95300 (H3.3) show distinct elemental and isotopic patterns.

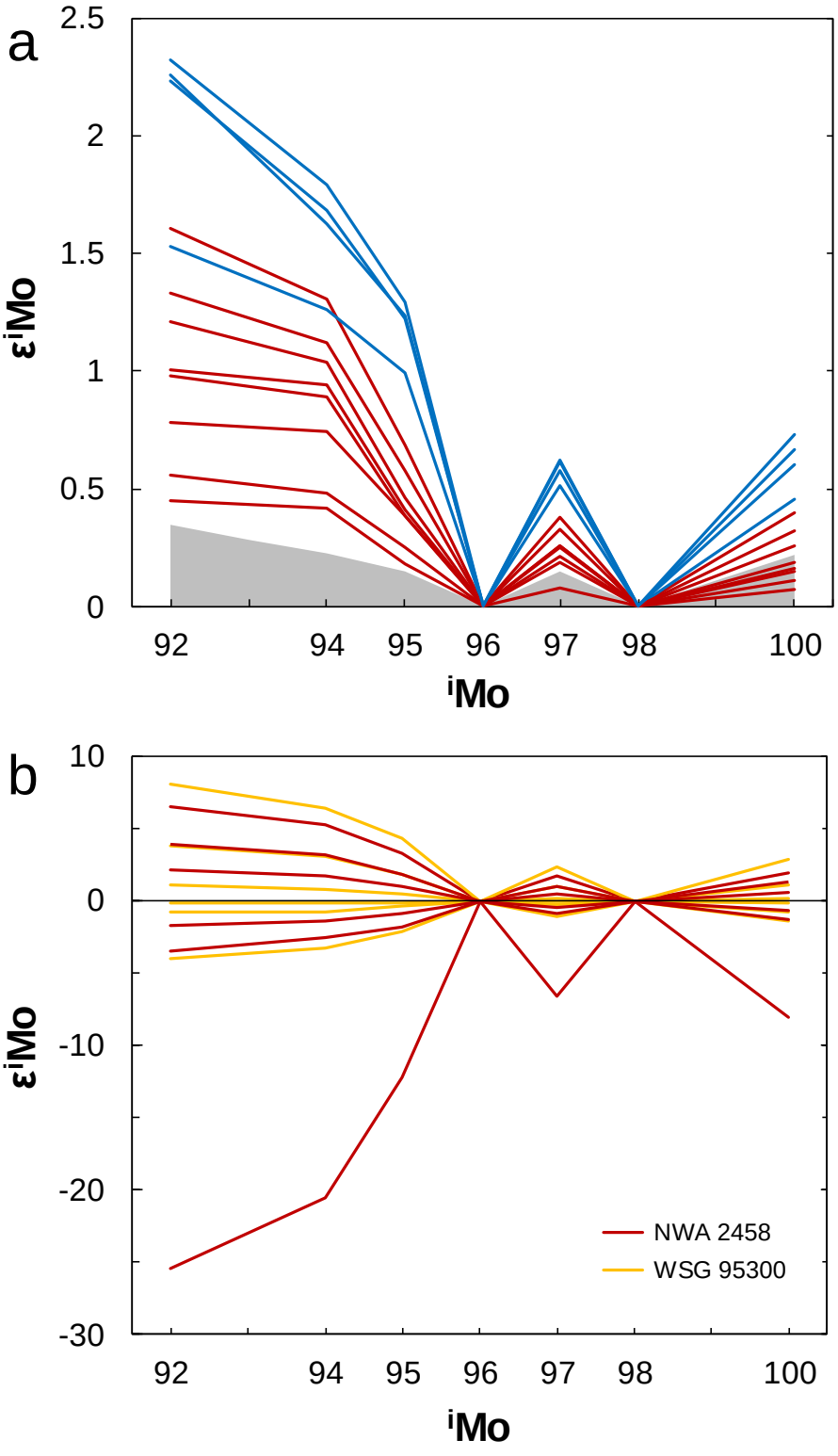

Supplementary Figure 4. Molybdenum isotope patterns of bulk meteorites (a) and acid leachates (b) from this study. All samples exhibit the typical *w*-shaped (or *m*-shaped) Mo isotope pattern indicative of a deficit (or excess) in *s*-process Mo nuclides.

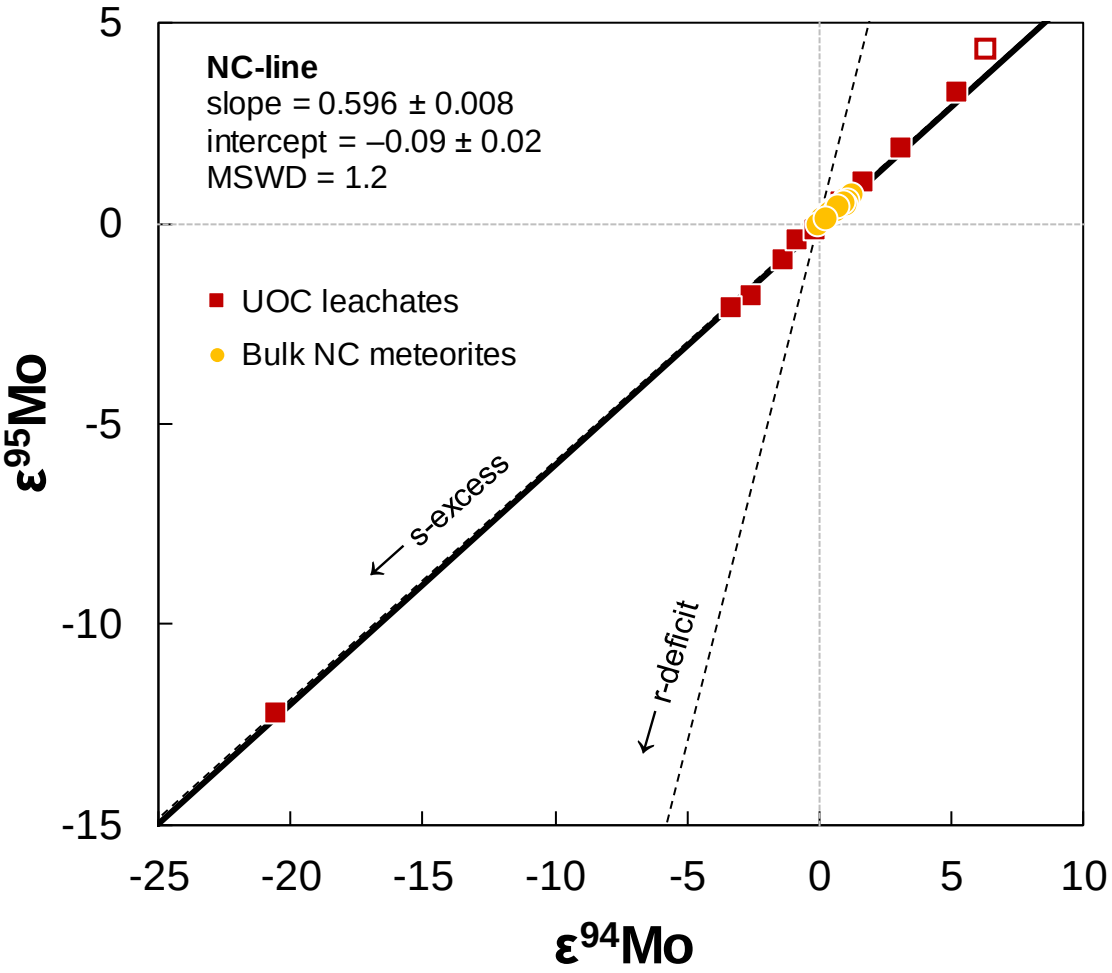

Supplementary Figure 5. Diagram of ε^{95}Mo versus ε^{94}Mo showing the combined regression of bulk (NC) meteorites and acid leachates from unequilibrated ordinary chondrites (NWA 2458, WSG 95300). This NC-line has a slope that is in excellent agreement with the predicted slope for *s*-process variability and a resolved negative *y*-axis intercept. Leachate step L6 from WSG 95300 (open symbol) was excluded from the regression (see Section S1).

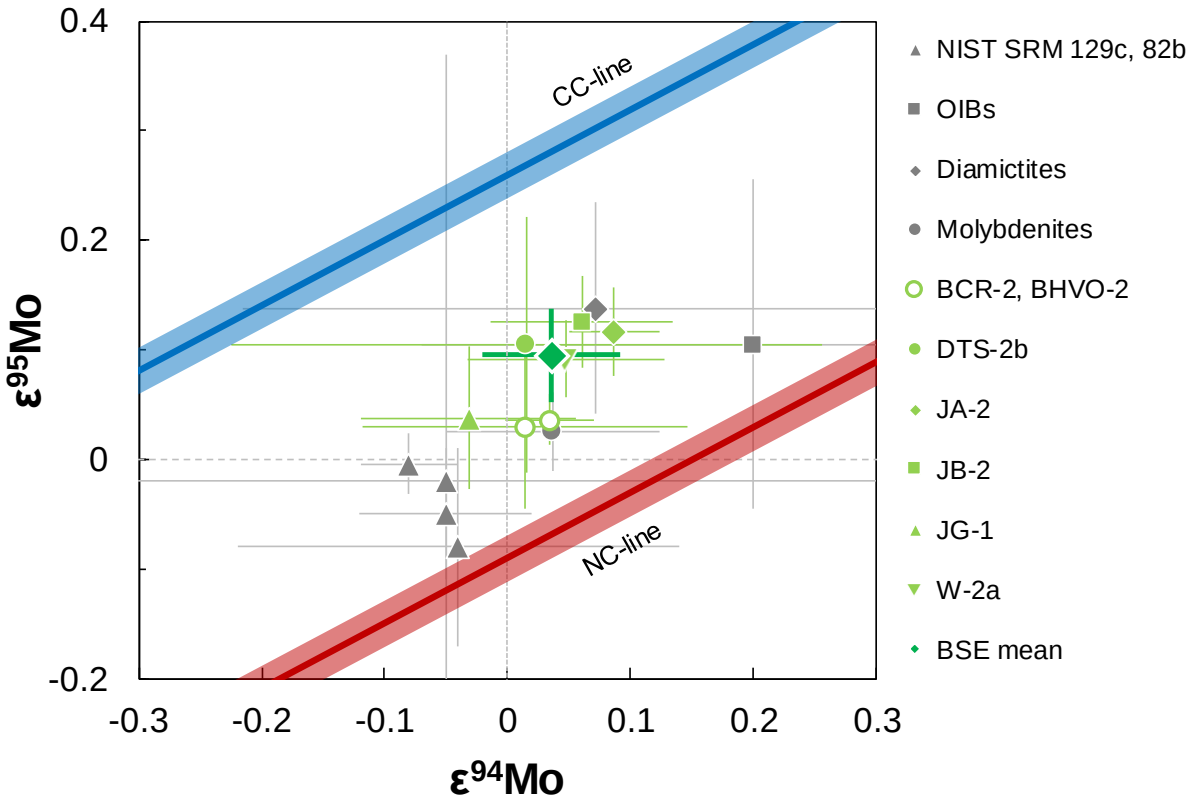

Supplementary Figure 6. Diagram of ε^{95}Mo versus ε^{94}Mo showing terrestrial samples relative to the CC- and NC-lines. Green symbols represent data from this study, grey symbols are literature data. Relative to the Mo solution standard (ε^{i}Mo ≡ 0), steel standards (NIST SRM 129c and 82b)[14,36,37] show slightly negative ε^{94}Mo and ε^{95}Mo. In contrast, the terrestrial rock standards analysed here (DTS-2b, JA-2, JB-2, JG-1, W-2a) as well as OIBs and diamictites from a previous study[11] show positive values. The (steel-contaminated) rock standards BHVO-2 and BCR-2 (open symbols) as well as molybdenites[11] plot closest to the solution standard. See Section S3 for details. Error bars typically represent 95% confidence intervals (95% CI).

Supplementary Table 1. Mo isotope data for meteoritic and terrestrial samples.

Sample		Weight (g)	Mo (µg/g)	N	ε^{92}Mo	ε^{94}Mo	ε^{95}Mo	ε^{97}Mo	ε^{100}Mo
Unprocessed solution standards									
Alfa Aesar (bracketing standard)		–	–		≡ 0	≡ 0	≡ 0	≡ 0	≡ 0
NIST SRM 3134		–	–	42	-0.04 ± 0.05	0.00 ± 0.04	0.01 ± 0.03	0.02 ± 0.02	-0.01 ± 0.03
Alfa Aesar Specpure Plasma		–	–	24	0.04 ± 0.10	0.04 ± 0.05	0.02 ± 0.04	0.00 ± 0.03	-0.01 ± 0.06
Processed solution standards									
Alfa Aesar (bracketing standard)		–	–	10	0.00 ± 0.15	-0.01 ± 0.11	0.03 ± 0.07	0.06 ± 0.03	0.00 ± 0.08
NIST SRM 3134		–	–	10	-0.02 ± 0.17	0.02 ± 0.11	0.05 ± 0.05	0.03 ± 0.06	-0.07 ± 0.07
Alfa Aesar (with DTS-2b matrix)		–	–	14	-0.01 ± 0.10	0.00 ± 0.06	0.03 ± 0.04	0.02 ± 0.05	-0.04 ± 0.04
Terrestrial rock samples									
BHVO-2	*OIB*	–	*4.07*	*40*	*0.01 ± 0.06*	*0.03 ± 0.04*	*0.04 ± 0.02*	*0.01 ± 0.02*	*-0.08 ± 0.04*
BCR-2	*Cont. flood basalt*	–	*250.6*	*10*	*-0.11 ± 0.14*	*0.01 ± 0.13*	*0.03 ± 0.07*	*0.02 ± 0.04*	*-0.08 ± 0.10*
JB-2	Arc basalt	–	1.014	15	0.11 ± 0.09	0.06 ± 0.07	0.13 ± 0.04	0.08 ± 0.04	-0.09 ± 0.05
JA-2	Andesite	–	0.581	17	0.17 ± 0.07	0.09 ± 0.04	0.12 ± 0.04	0.04 ± 0.04	-0.03 ± 0.07
JG-1	Granodiorite	–	1.54	7	-0.10 ± 0.12	-0.03 ± 0.09	0.04 ± 0.07	0.07 ± 0.05	-0.05 ± 0.09
W-2a	Diabase	–	0.465	10	0.08 ± 0.12	0.05 ± 0.08	0.09 ± 0.04	0.05 ± 0.03	-0.08 ± 0.06
DTS-2b	Dunite	–	0.057	4	0.13 ± 0.38	0.02 ± 0.24	0.10 ± 0.12	0.06 ± 0.09	-0.08 ± 0.31
Bulk silicate Earth	*(±95% CI)*	–	–	–	*0.08 ± 0.13*	*0.04 ± 0.06*	*0.10 ± 0.04*	*0.06 ± 0.02*	*-0.07 ± 0.04*
Bulk meteorites									
CK chondrites	NWA 6604	0.556	0.45	3	2.26 ± 0.35	1.63 ± 0.22	1.24 ± 0.15	0.58 ± 0.15	0.73 ± 0.22
CH chondrites	Acfer 182	0.553	1.60	6	2.32 ± 0.11	1.79 ± 0.10	1.29 ± 0.04	0.62 ± 0.09	0.66 ± 0.11
CB chondrites	HaH 237	0.561	3.23	9	1.53 ± 0.08	1.26 ± 0.04	0.99 ± 0.04	0.51 ± 0.04	0.45 ± 0.04
Rumuruti chondrites	NWA 053	0.564	0.92	4	0.35 ± 0.18	0.33 ± 0.12	0.15 ± 0.06	0.06 ± 0.06	0.07 ± 0.19
	NWA 753	0.559	0.57	3	0.72 ± 0.35	0.65 ± 0.22	0.31 ± 0.15	0.19 ± 0.15	0.17 ± 0.22
	NWA 6145	0.450	0.72	3	0.53 ± 0.35	0.49 ± 0.22	0.23 ± 0.15	0.09 ± 0.15	0.12 ± 0.22
	Weighted Average	–	–	–	*0.45 ± 0.15*	*0.42 ± 0.10*	*0.18 ± 0.05*	*0.08 ± 0.05*	*0.11 ± 0.12*
Acapulcoites	Dho 125	0.535	0.91	5	1.01 ± 0.24	0.94 ± 0.12	0.41 ± 0.07	0.26 ± 0.08	0.26 ± 0.11
Brachinites	NWA 3151	0.531	0.47	3	1.29 ± 0.35	1.14 ± 0.22	0.61 ± 0.15	0.36 ± 0.15	0.38 ± 0.22
	NWA 4882	1.102	0.38	4	1.34 ± 0.16	1.10 ± 0.21	0.56 ± 0.11	0.32 ± 0.04	0.31 ± 0.10
	Weighted Average	–	–	–	*1.33 ± 0.15*	*1.12 ± 0.15*	*0.58 ± 0.08*	*0.33 ± 0.04*	*0.32 ± 0.09*
Ureilites	Dho 1519	0.820	0.76	4	0.64 ± 0.19	0.61 ± 0.14	0.32 ± 0.10	0.22 ± 0.08	0.03 ± 0.12
	NWA 7630	0.798	0.53	3	1.06 ± 0.35	1.01 ± 0.22	0.44 ± 0.15	0.26 ± 0.15	0.26 ± 0.22
	ALHA77257	1.240	0.22	2	0.74 ± 0.35	0.79 ± 0.22	0.26 ± 0.15	0.15 ± 0.15	0.00 ± 0.22
	EET 87720	1.236	0.12	1	1.02 ± 0.35	0.79 ± 0.22	0.38 ± 0.15	0.23 ± 0.15	0.35 ± 0.22
	EET 96042	0.759	0.39	2	1.14 ± 0.35	1.10 ± 0.22	0.42 ± 0.15	0.21 ± 0.15	0.19 ± 0.22
	GRA 95205	0.877	0.48	3	1.15 ± 0.35	1.00 ± 0.22	0.43 ± 0.15	0.32 ± 0.15	0.28 ± 0.22
	LAP 03721	1.253	0.20	1	0.91 ± 0.35	0.87 ± 0.22	0.37 ± 0.15	0.13 ± 0.15	0.10 ± 0.22
	LAR 04315	1.234	0.29	2	1.12 ± 0.35	0.99 ± 0.22	0.34 ± 0.15	0.14 ± 0.15	0.22 ± 0.22
	MIL 090031	1.118	0.30	3	1.18 ± 0.35	1.05 ± 0.22	0.45 ± 0.15	0.25 ± 0.15	0.20 ± 0.22
	GRO 95575	1.275	0.16	1	1.17 ± 0.35	1.07 ± 0.22	0.47 ± 0.15	0.30 ± 0.15	0.21 ± 0.22
	NWA 3140	0.512	0.30	1	0.98 ± 0.35	0.86 ± 0.22	0.42 ± 0.15	0.23 ± 0.15	-0.09 ± 0.22
	NWA 3156	0.676	0.32	1	0.83 ± 0.35	0.72 ± 0.22	0.24 ± 0.15	0.23 ± 0.15	0.07 ± 0.22
	NWA 7276	1.284	0.24	2	0.65 ± 0.35	0.68 ± 0.22	0.29 ± 0.15	0.16 ± 0.15	0.00 ± 0.22
	Dho 132	1.437	0.34	3	0.66 ± 0.35	0.65 ± 0.22	0.35 ± 0.15	0.22 ± 0.15	0.11 ± 0.22
	MS-MU-17	0.930	0.13	1	1.08 ± 0.35	0.93 ± 0.22	0.42 ± 0.15	0.13 ± 0.15	0.30 ± 0.22
	MS-MU-20	0.963	0.32	2	1.40 ± 0.35	1.15 ± 0.22	0.51 ± 0.15	0.25 ± 0.15	0.20 ± 0.22
	EET 87517	*1.091*	*0.38*	*2*	*1.90 ± 0.35*	*1.62 ± 0.22*	*0.83 ± 0.15*	*0.48 ± 0.15*	*0.47 ± 0.22*
	PCA 82506	*1.081*	*0.21*	*1*	*2.04 ± 0.35*	*1.35 ± 0.22*	*0.73 ± 0.15*	*0.30 ± 0.15*	*0.40 ± 0.22*
	Weighted Average	–	–	–	*0.98 ± 0.12*	*0.89 ± 0.09*	*0.38 ± 0.04*	*0.21 ± 0.03*	*0.15 ± 0.07*
Mesosiderites	Acfer 063	0.399	2.37	6	1.23 ± 0.21	1.05 ± 0.12	0.46 ± 0.07	0.26 ± 0.04	0.21 ± 0.09
	Ilafegh 002	0.336	2.43	7	1.16 ± 0.23	1.01 ± 0.16	0.45 ± 0.12	0.26 ± 0.08	0.18 ± 0.05
	NWA 2538	0.328	1.81	5	1.27 ± 0.34	1.04 ± 0.17	0.49 ± 0.12	0.24 ± 0.06	0.23 ± 0.14
	Weighted Average	–	–	–	*1.21 ± 0.14*	*1.04 ± 0.08*	*0.46 ± 0.05*	*0.25 ± 0.03*	*0.19 ± 0.04*
Angrites	NWA 4931	2.210	0.31	5	0.78 ± 0.28	0.75 ± 0.11	0.39 ± 0.06	0.26 ± 0.10	0.07 ± 0.12
Aubrites	Peña Blanca Spring	10.50	0.01	1	0.50 ± 0.35	0.58 ± 0.22	0.16 ± 0.15	0.07 ± 0.15	0.16 ± 0.22
	Norton County (metal)	0.501	2.85	6	0.57 ± 0.14	0.47 ± 0.05	0.26 ± 0.06	0.19 ± 0.03	0.17 ± 0.11
	Weighted Average	–	–	–	*0.56 ± 0.13*	*0.48 ± 0.05*	*0.25 ± 0.06*	*0.19 ± 0.03*	*0.16 ± 0.10*
Tafassasset (metal)	(ungr. achondrite)	0.418	8.25	7	2.17 ± 0.15	1.65 ± 0.07	1.20 ± 0.05	0.62 ± 0.05	0.63 ± 0.06
NWA 1058	(ungr. achondrite)	0.514	1.41	6	1.61 ± 0.12	1.31 ± 0.11	0.68 ± 0.09	0.38 ± 0.10	0.40 ± 0.08

Supplementary Table 1. *Continued*.

Sample		Weight (g)	Mo (µg/g)	N	ε^{92}Mo	ε^{94}Mo	ε^{95}Mo	ε^{97}Mo	ε^{100}Mo
Acid leachates									
NWA 2458	L1	–	(156)	1	6.47 ± 0.35	5.30 ± 0.22	3.25 ± 0.15	1.76 ± 0.15	1.93 ± 0.22
(L3.2)	L2	–	(2078)	6	3.90 ± 0.20	3.18 ± 0.08	1.87 ± 0.09	0.98 ± 0.05	1.28 ± 0.07
	L3	–	(301)	2	2.13 ± 0.35	1.70 ± 0.22	1.00 ± 0.15	0.53 ± 0.15	0.55 ± 0.22
	L4	–	(495)	4	-3.45 ± 0.31	-2.57 ± 0.28	-1.82 ± 0.15	-0.90 ± 0.07	-1.24 ± 0.07
	L5	–	(737)	5	-1.69 ± 0.36	-1.36 ± 0.24	-0.89 ± 0.14	-0.50 ± 0.04	-0.71 ± 0.07
	L6	–	(192)	2	-25.43 ± 0.35	-20.53 ± 0.22	-12.22 ± 0.15	-6.55 ± 0.15	-8.04 ± 0.22
	Total / Wtd. Average	–	*(3958)*	–	*0.49*	*0.44*	*0.20*	*0.10*	*0.11*
	Whole rock	0.668	0.67	4	0.42 ± 0.32	0.37 ± 0.28	0.21 ± 0.17	0.16 ± 0.07	0.02 ± 0.09
WSG 95300	L1	–	(98)	1	-0.74 ± 0.35	-0.76 ± 0.22	-0.40 ± 0.15	-0.27 ± 0.15	-0.74 ± 0.22
(H3.3)	L2	–	(1198)	4	1.10 ± 0.04	0.83 ± 0.13	0.52 ± 0.04	0.21 ± 0.07	0.16 ± 0.09
	L3	–	(523)	4	-4.03 ± 0.36	-3.30 ± 0.24	-2.10 ± 0.15	-1.12 ± 0.07	-1.39 ± 0.15
	L4	–	(1187)	6	-0.15 ± 0.24	-0.10 ± 0.14	-0.17 ± 0.12	-0.02 ± 0.07	-0.19 ± 0.17
	L5	–	(2021)	6	3.81 ± 0.14	3.13 ± 0.11	1.89 ± 0.10	0.98 ± 0.10	1.09 ± 0.11
	L6	–	(109)	1	8.09 ± 0.35	6.40 ± 0.22	4.32 ± 0.15	2.37 ± 0.15	2.88 ± 0.22
	Total / Wtd. Average	–	*(5137)*	–	*1.47*	*1.19*	*0.69*	*0.36*	*0.33*

Mo isotope ratios are normalized to ^{98}Mo/^{96}Mo = 1.453173 and reported relative to the Alfa Aesar bracketing standard. Given uncertainties represent the external reproducibility (2 s.d.) obtained from repeated analyses of BHVO-2 (Supplementary Table 2) or 95% confidence intervals (95% CI) for samples with N>3 (N: number of analyses). BHVO-2 and BCR-2 are not included in the BSE mean (see Section S3); EET 87517 and PCA 82506 are distinct from other ureilites and thus not included in the group mean. Mo concentrations were determined by quadrupole ICP-MS, which have an uncertainty of ~5%; values for rock standards are from GeoReM database; for acid leachates the amount of Mo (ng) released in the respective step is reported (values in parentheses).

Supplementary Table 2. Mo isotope data for terrestrial rock standards.

Sample / ID	ε^{92}Mo (± 2 s.e.)	ε^{94}Mo (± 2 s.e.)	ε^{95}Mo (± 2 s.e.)	ε^{97}Mo (± 2 s.e.)	ε^{100}Mo (± 2 s.e.)
BHVO-2					
BHV22.1	-0.34 ± 0.19	-0.08 ± 0.13	-0.03 ± 0.10	-0.02 ± 0.08	-0.06 ± 0.12
BHV22.2	0.25 ± 0.23	0.17 ± 0.17	0.02 ± 0.12	0.00 ± 0.08	-0.02 ± 0.14
BHV22.3	-0.13 ± 0.22	-0.05 ± 0.15	0.02 ± 0.11	0.08 ± 0.09	-0.02 ± 0.13
BHV22.4	0.06 ± 0.20	0.08 ± 0.17	-0.03 ± 0.11	-0.10 ± 0.09	-0.08 ± 0.13
BHV22.5	-0.06 ± 0.20	-0.11 ± 0.12	0.02 ± 0.10	0.01 ± 0.07	-0.24 ± 0.11
BHV22.6	0.21 ± 0.18	0.13 ± 0.13	0.11 ± 0.09	0.03 ± 0.09	-0.19 ± 0.12
BHV22.7	-0.11 ± 0.22	0.03 ± 0.15	-0.02 ± 0.12	-0.05 ± 0.08	-0.12 ± 0.14
BHV22.8	0.01 ± 0.21	0.12 ± 0.15	0.01 ± 0.11	0.06 ± 0.09	-0.06 ± 0.12
BHV23.1	-0.09 ± 0.22	0.14 ± 0.13	0.02 ± 0.09	0.01 ± 0.08	-0.01 ± 0.14
BHV23.2	0.22 ± 0.22	0.14 ± 0.15	0.08 ± 0.10	0.05 ± 0.07	-0.30 ± 0.13
BHV23.3	0.32 ± 0.19	0.10 ± 0.15	0.05 ± 0.09	-0.06 ± 0.09	-0.19 ± 0.11
BHV23.4	0.04 ± 0.20	-0.01 ± 0.15	0.00 ± 0.12	-0.12 ± 0.09	-0.26 ± 0.13
BHV23.5	-0.10 ± 0.18	-0.04 ± 0.13	0.03 ± 0.09	0.02 ± 0.08	-0.12 ± 0.12
BHV23.6	-0.08 ± 0.20	-0.01 ± 0.14	0.02 ± 0.09	0.04 ± 0.07	-0.05 ± 0.11
BHV23.7	-0.04 ± 0.23	0.04 ± 0.15	0.06 ± 0.12	-0.05 ± 0.08	-0.17 ± 0.13
BHV23.8	0.05 ± 0.19	0.12 ± 0.13	0.08 ± 0.09	0.06 ± 0.08	0.08 ± 0.13
BHV24.1	-0.02 ± 0.15	0.13 ± 0.10	0.05 ± 0.08	0.05 ± 0.07	-0.24 ± 0.11
BHV24.2	-0.12 ± 0.21	-0.04 ± 0.13	-0.05 ± 0.11	-0.07 ± 0.07	0.03 ± 0.13
BHV24.3	-0.08 ± 0.20	-0.14 ± 0.13	-0.01 ± 0.10	-0.14 ± 0.09	0.08 ± 0.10
BHV24.4	0.13 ± 0.22	0.03 ± 0.14	0.11 ± 0.11	0.03 ± 0.07	-0.16 ± 0.14
BHV24.5	0.01 ± 0.16	0.03 ± 0.12	0.07 ± 0.09	-0.09 ± 0.08	-0.03 ± 0.12
BHV24.6	0.13 ± 0.21	0.07 ± 0.14	0.09 ± 0.11	0.01 ± 0.09	-0.19 ± 0.13
BHV24.7	0.01 ± 0.18	0.07 ± 0.14	0.10 ± 0.10	0.09 ± 0.08	-0.14 ± 0.12
BHV24.8	-0.09 ± 0.20	-0.13 ± 0.13	-0.03 ± 0.10	0.13 ± 0.09	-0.06 ± 0.12
BHV25.1	0.27 ± 0.18	0.27 ± 0.13	0.13 ± 0.09	0.03 ± 0.07	-0.13 ± 0.10
BHV25.2	0.27 ± 0.19	0.01 ± 0.13	0.10 ± 0.10	-0.09 ± 0.08	-0.15 ± 0.12
BHV25.3	-0.27 ± 0.18	-0.06 ± 0.13	-0.10 ± 0.09	-0.02 ± 0.08	0.16 ± 0.12
BHV25.4	0.02 ± 0.20	0.07 ± 0.14	0.15 ± 0.10	0.10 ± 0.08	0.01 ± 0.14
BHV25.5	0.22 ± 0.19	0.21 ± 0.14	0.13 ± 0.10	-0.10 ± 0.09	-0.05 ± 0.11
BHV25.6	-0.30 ± 0.21	-0.13 ± 0.14	-0.03 ± 0.10	0.00 ± 0.08	0.09 ± 0.13
BHV25.7	-0.05 ± 0.21	-0.03 ± 0.14	0.02 ± 0.10	0.10 ± 0.08	-0.04 ± 0.11
BHV25.8	-0.04 ± 0.17	-0.04 ± 0.13	-0.05 ± 0.09	0.09 ± 0.06	0.01 ± 0.13
BHV26.10	-0.24 ± 0.22	-0.07 ± 0.14	-0.09 ± 0.11	0.00 ± 0.07	0.00 ± 0.12
BHV26.11	0.04 ± 0.19	0.04 ± 0.13	-0.04 ± 0.09	-0.03 ± 0.07	-0.22 ± 0.12
BHV26.12	0.08 ± 0.23	0.14 ± 0.14	0.11 ± 0.12	-0.08 ± 0.08	-0.10 ± 0.12
BHV26.13	0.12 ± 0.20	0.08 ± 0.15	0.08 ± 0.11	-0.01 ± 0.09	-0.09 ± 0.12
BHV26.14	-0.04 ± 0.21	-0.07 ± 0.14	-0.04 ± 0.10	0.06 ± 0.09	-0.09 ± 0.12
BHV26.15	0.22 ± 0.18	0.08 ± 0.14	0.23 ± 0.10	0.16 ± 0.09	0.03 ± 0.12
BHV26.16	0.25 ± 0.21	0.27 ± 0.13	0.11 ± 0.10	0.17 ± 0.09	-0.14 ± 0.12
BHV26.17	-0.35 ± 0.20	-0.22 ± 0.17	-0.05 ± 0.12	0.01 ± 0.09	0.13 ± 0.13
N	40	40	40	40	40
Mean	0.01	0.03	0.04	0.01	-0.08
2 s.d.	0.35	0.22	0.15	0.15	0.22
95% CI	0.06	0.04	0.02	0.02	0.04
BCR-2					
BCR_A.1	-0.15 ± 0.24	-0.02 ± 0.17	-0.07 ± 0.11	-0.05 ± 0.08	-0.04 ± 0.15
BCR_A.2	-0.32 ± 0.19	-0.15 ± 0.16	-0.05 ± 0.10	-0.07 ± 0.08	0.05 ± 0.12
BCR_A.3	0.14 ± 0.20	0.13 ± 0.14	0.18 ± 0.09	0.01 ± 0.09	-0.12 ± 0.13
BCR_A.4	-0.32 ± 0.22	-0.23 ± 0.15	-0.15 ± 0.11	0.03 ± 0.10	0.00 ± 0.13
BCR_A.5	-0.13 ± 0.20	-0.09 ± 0.13	0.01 ± 0.11	0.00 ± 0.08	-0.16 ± 0.14
BCR_A.6	0.06 ± 0.21	0.21 ± 0.15	0.14 ± 0.09	0.06 ± 0.07	-0.23 ± 0.13
BCR_A.7	0.05 ± 0.19	0.33 ± 0.14	0.10 ± 0.10	0.00 ± 0.08	-0.24 ± 0.12
BCR_A.8	0.03 ± 0.20	0.17 ± 0.15	0.09 ± 0.12	0.04 ± 0.08	0.05 ± 0.12
BCR_A.9	-0.46 ± 0.20	-0.18 ± 0.15	-0.02 ± 0.10	0.14 ± 0.08	0.12 ± 0.12
BCR_A.10	0.01 ± 0.18	-0.04 ± 0.13	0.07 ± 0.10	0.04 ± 0.09	-0.28 ± 0.13
DTS-2b					
DTS39	0.26 ± 0.24	0.04 ± 0.16	0.10 ± 0.11	0.06 ± 0.08	-0.30 ± 0.15
DTS44.1	-0.06 ± 0.22	-0.18 ± 0.15	0.05 ± 0.11	0.00 ± 0.09	0.17 ± 0.16
DTS44.2	0.40 ± 0.25	0.19 ± 0.17	0.21 ± 0.11	0.03 ± 0.11	-0.14 ± 0.14
DTS44.3	-0.08 ± 0.24	0.01 ± 0.15	0.05 ± 0.11	0.14 ± 0.08	-0.06 ± 0.15

Supplementary Table 2. *Continued*.

Sample / ID	ε^{92}Mo (± 2 s.e.)	ε^{94}Mo (± 2 s.e.)	ε^{95}Mo (± 2 s.e.)	ε^{97}Mo (± 2 s.e.)	ε^{100}Mo (± 2 s.e.)
JB-2					
JB201.1	-0.04 ± 0.18	0.12 ± 0.11	0.08 ± 0.10	0.06 ± 0.07	0.00 ± 0.13
JB201.2	0.21 ± 0.20	0.27 ± 0.15	0.23 ± 0.09	0.14 ± 0.08	-0.16 ± 0.13
JB201.3	0.42 ± 0.18	0.26 ± 0.14	0.21 ± 0.09	0.14 ± 0.08	-0.27 ± 0.12
JB201.4	-0.15 ± 0.20	-0.18 ± 0.14	0.09 ± 0.10	0.01 ± 0.08	-0.08 ± 0.14
JB201.5	0.02 ± 0.21	-0.01 ± 0.14	0.10 ± 0.10	0.05 ± 0.08	0.02 ± 0.13
JB201.6	0.01 ± 0.21	0.06 ± 0.16	0.14 ± 0.11	0.16 ± 0.08	0.00 ± 0.13
JB201.7	0.18 ± 0.19	0.00 ± 0.13	0.12 ± 0.10	0.03 ± 0.08	-0.03 ± 0.14
JB202.1	0.06 ± 0.17	-0.04 ± 0.12	0.13 ± 0.09	0.03 ± 0.08	-0.13 ± 0.13
JB202.2	0.27 ± 0.21	0.05 ± 0.17	0.29 ± 0.10	0.16 ± 0.08	-0.18 ± 0.12
JB202.3	0.07 ± 0.21	0.14 ± 0.12	0.07 ± 0.11	0.18 ± 0.09	-0.15 ± 0.12
JB202.4	0.07 ± 0.20	-0.02 ± 0.15	0.15 ± 0.10	0.03 ± 0.08	-0.09 ± 0.12
JB204.1	0.03 ± 0.23	-0.02 ± 0.17	-0.01 ± 0.11	-0.03 ± 0.07	0.00 ± 0.12
JB204.2	0.38 ± 0.22	0.26 ± 0.16	0.16 ± 0.12	0.13 ± 0.08	-0.18 ± 0.13
JB204.3	-0.06 ± 0.22	0.12 ± 0.16	0.07 ± 0.10	0.04 ± 0.10	-0.08 ± 0.14
JB204.4	0.11 ± 0.20	-0.10 ± 0.14	0.07 ± 0.10	0.04 ± 0.08	-0.09 ± 0.13
JA-2					
JA2.1	0.27 ± 0.21	0.07 ± 0.16	0.11 ± 0.11	0.07 ± 0.08	-0.04 ± 0.12
JA2.2	-0.10 ± 0.19	-0.03 ± 0.13	0.00 ± 0.09	-0.01 ± 0.09	0.05 ± 0.14
JA2.3	0.33 ± 0.23	0.14 ± 0.16	0.15 ± 0.12	0.02 ± 0.09	-0.06 ± 0.14
JA2.4	0.24 ± 0.21	0.22 ± 0.15	0.16 ± 0.11	0.13 ± 0.08	0.01 ± 0.13
JA2.5	0.19 ± 0.21	0.01 ± 0.16	0.10 ± 0.10	0.08 ± 0.09	-0.01 ± 0.13
JA2.6	0.00 ± 0.20	0.15 ± 0.14	0.07 ± 0.11	0.00 ± 0.08	0.11 ± 0.13
JA2.7	0.14 ± 0.21	0.00 ± 0.14	0.09 ± 0.12	0.13 ± 0.10	-0.20 ± 0.12
JA2.8	0.31 ± 0.19	0.16 ± 0.14	0.14 ± 0.11	-0.02 ± 0.08	-0.21 ± 0.13
JA2.9	0.01 ± 0.23	0.03 ± 0.15	0.11 ± 0.12	-0.02 ± 0.08	0.06 ± 0.14
JA2.10	0.25 ± 0.20	0.07 ± 0.13	0.16 ± 0.10	-0.07 ± 0.09	-0.05 ± 0.11
JA2.11	0.20 ± 0.21	0.06 ± 0.13	0.11 ± 0.10	0.05 ± 0.08	0.16 ± 0.13
DI36.1	0.40 ± 0.19	0.13 ± 0.12	0.30 ± 0.10	0.10 ± 0.08	-0.22 ± 0.14
DI36.2	0.15 ± 0.22	0.05 ± 0.13	0.24 ± 0.10	0.10 ± 0.08	-0.12 ± 0.15
DI36.3	0.11 ± 0.20	0.14 ± 0.11	0.16 ± 0.08	0.13 ± 0.08	-0.23 ± 0.13
DI36.4	0.33 ± 0.21	0.18 ± 0.14	0.04 ± 0.12	0.04 ± 0.09	-0.07 ± 0.14
DI36.5	0.01 ± 0.22	0.02 ± 0.16	-0.02 ± 0.11	0.08 ± 0.09	0.23 ± 0.14
DI36.6	0.05 ± 0.22	0.08 ± 0.17	0.06 ± 0.12	-0.09 ± 0.10	0.14 ± 0.15
JG-1					
DI35.1	-0.13 ± 0.23	0.06 ± 0.17	0.02 ± 0.10	0.11 ± 0.08	-0.04 ± 0.12
DI35.2	-0.11 ± 0.21	-0.05 ± 0.14	0.06 ± 0.09	0.11 ± 0.08	-0.13 ± 0.12
DI35.3	-0.07 ± 0.18	-0.06 ± 0.12	0.14 ± 0.10	0.03 ± 0.08	-0.03 ± 0.14
DI35.4	0.02 ± 0.21	0.06 ± 0.16	0.06 ± 0.12	0.15 ± 0.08	-0.17 ± 0.13
DI35.5	-0.25 ± 0.19	0.00 ± 0.13	-0.02 ± 0.10	-0.02 ± 0.09	-0.08 ± 0.12
DI35.6	0.07 ± 0.17	0.00 ± 0.13	0.09 ± 0.10	0.03 ± 0.07	-0.03 ± 0.11
DI35.7	-0.27 ± 0.18	-0.22 ± 0.12	-0.08 ± 0.10	0.06 ± 0.07	0.15 ± 0.13
W-2a					
W2a.1	0.32 ± 0.21	0.26 ± 0.14	0.09 ± 0.10	0.04 ± 0.09	0.00 ± 0.13
W2a.2	0.00 ± 0.20	0.00 ± 0.13	0.07 ± 0.09	0.05 ± 0.07	-0.13 ± 0.13
W2a.3	0.30 ± 0.20	0.14 ± 0.15	0.12 ± 0.10	0.07 ± 0.08	-0.22 ± 0.12
W2a.4	0.22 ± 0.22	0.13 ± 0.17	0.09 ± 0.10	0.13 ± 0.08	-0.15 ± 0.12
W2a.5	0.00 ± 0.21	0.04 ± 0.15	0.12 ± 0.11	0.04 ± 0.09	-0.09 ± 0.14
W2a.6	-0.07 ± 0.22	-0.03 ± 0.16	0.05 ± 0.10	0.04 ± 0.08	-0.17 ± 0.14
W2a.7	0.14 ± 0.20	-0.02 ± 0.15	0.14 ± 0.10	0.00 ± 0.10	-0.02 ± 0.13
W2a.8	0.02 ± 0.19	0.06 ± 0.14	0.17 ± 0.11	0.10 ± 0.10	-0.01 ± 0.12
W2a.9	-0.24 ± 0.20	-0.15 ± 0.14	0.00 ± 0.10	0.00 ± 0.08	0.00 ± 0.12
W2a.10	0.12 ± 0.22	0.05 ± 0.14	0.06 ± 0.10	0.04 ± 0.08	-0.03 ± 0.15

Mo isotope ratios are normalized to $^{98}Mo/^{96}Mo$ = 1.453173 and reported relative to the Alfa Aesar bracketing standard. Each line represents a single measurement, which consumed ~80 ng of Mo (run at ~100 ppb). Given uncertainties are two standard errors (2 s.e.) obtained from internal run statistics. BHVO-2: Different numbers (22–26) denote separate digestions of ~0.5 g standard material that were processed through the full chemical separation procedure and analysed with each set of samples. Mean values (±95% CI) for the different rock standards are provided in Supplementary Table 1.

Supplementary Table 3. Leaching procedure applied to the unequilibrated ordinary chondrites NWA 2458 (L3.2) and WSG 95300 (H3.3).

Step	Acid volumes	Acid mixture	Temperature (°C)	Duration (days)
L1	25ml HAc + 25ml H2O	50ml 8.9M HAc	20	1
L2	12.5ml HNO3 + 25ml H2O	37.5ml 5.1M HNO3	20	5
L3	15ml HCl + 17.5ml H2O	32.5ml 5.0M HCl	75	1
L4	15ml HF + 7.5ml HCl + 7.5ml H2O	30ml 14.6M HF – 2.7M HCl	75	1
L5	7.5ml HF + 7.5ml HCl	15ml 14.6M HF – 5.5M HCl	150	3
L6a	14ml HF + 7ml HNO3 + 0.4ml HClO4	21.4ml 19.0M HF – 5.0M HNO3 – 2% HClO4	180-200	5
L6b	14ml HNO3 + 7ml HCl	21ml 10.3M HNO3 – 3.7M HCl	130-170	3

The procedure was modified from ref. 35. See Methods for details.

Supplementary Table 4. Summary of Mo isotope data for bulk meteorites.

Sample	ε^{92}Mo	ε^{94}Mo	ε^{95}Mo	ε^{97}Mo	ε^{100}Mo	Reference
Carbonaceous meteorites						
CI	1.12 ± 0.59	0.79 ± 0.41	0.69 ± 0.23	0.26 ± 0.19	0.44 ± 0.34	37
CM	6.44 ± 0.39	4.82 ± 0.20	3.17 ± 0.16	1.66 ± 0.14	2.28 ± 0.22	37
CO	2.41 ± 0.15	1.66 ± 0.34	1.39 ± 0.34	0.71 ± 0.28	0.97 ± 0.11	47
CV	1.41 ± 0.27	0.97 ± 0.19	0.81 ± 0.05	0.40 ± 0.08	0.44 ± 0.12	12
CK	2.26 ± 0.35	1.63 ± 0.22	1.24 ± 0.15	0.58 ± 0.15	0.73 ± 0.22	this study
CR	4.14 ± 0.12	3.11 ± 0.15	2.26 ± 0.04	1.18 ± 0.04	1.40 ± 0.17	36
CH	2.32 ± 0.11	1.79 ± 0.10	1.29 ± 0.04	0.62 ± 0.09	0.66 ± 0.11	this study
CB	1.53 ± 0.08	1.26 ± 0.04	0.99 ± 0.04	0.51 ± 0.04	0.45 ± 0.04	this study
Eagle Station pallasites	1.14 ± 0.24	0.85 ± 0.32	0.80 ± 0.14	0.41 ± 0.09	0.79 ± 0.15	37
Milton (ungr.)	–	1.30 ± 0.26	1.04 ± 0.09	0.54 ± 0.05	–	48
Tafassasset (ungr.)	2.17 ± 0.15	1.65 ± 0.07	1.20 ± 0.05	0.62 ± 0.05	0.63 ± 0.06	this study
IIC	3.11 ± 0.12	2.22 ± 0.09	1.54 ± 0.06	0.85 ± 0.07	0.96 ± 0.07	13
IID	1.63 ± 0.10	1.16 ± 0.16	0.96 ± 0.15	0.51 ± 0.12	0.67 ± 0.17	13
IIF	1.50 ± 0.21	1.11 ± 0.13	0.94 ± 0.08	0.50 ± 0.08	0.63 ± 0.13	13
IIIF	1.59 ± 0.14	1.20 ± 0.11	0.99 ± 0.04	0.55 ± 0.06	0.61 ± 0.09	13
IVB	2.47 ± 0.76	1.55 ± 0.22	1.17 ± 0.10	0.57 ± 0.03	0.84 ± 0.33	15
South Byron Trio (SBT)	–	1.27 ± 0.07	1.03 ± 0.04	0.49 ± 0.02	–	48
Grand Rapids (ungr.)	1.28 ± 0.62	1.15 ± 0.40	0.89 ± 0.25	0.45 ± 0.25	0.48 ± 0.36	49
Mbosi (ungr.)	1.17 ± 0.67	1.10 ± 0.43	1.02 ± 0.27	0.50 ± 0.20	0.63 ± 0.25	37
Wiley (ungr.)	4.47 ± 0.22	3.49 ± 0.13	2.34 ± 0.11	1.21 ± 0.11	1.41 ± 0.14	13
Non-carbonaceous meteorites						
OC	0.66 ± 0.08	0.61 ± 0.06	0.25 ± 0.06	0.11 ± 0.05	0.14 ± 0.08	50
EC	0.38 ± 0.06	0.36 ± 0.05	0.14 ± 0.03	0.09 ± 0.02	0.14 ± 0.03	50
RC	0.45 ± 0.15	0.42 ± 0.10	0.18 ± 0.05	0.08 ± 0.05	0.11 ± 0.12	this study
Acapulcoites	1.01 ± 0.24	0.94 ± 0.12	0.41 ± 0.07	0.26 ± 0.08	0.26 ± 0.11	this study
Lodranites	1.48 ± 0.90	1.10 ± 0.30	0.48 ± 0.15	0.21 ± 0.03	0.24 ± 0.22	15
Winonaites	0.30 ± 0.28	0.22 ± 0.10	0.07 ± 0.04	0.02 ± 0.09	0.03 ± 0.06	15
Brachinites	1.33 ± 0.15	1.12 ± 0.15	0.58 ± 0.08	0.33 ± 0.04	0.32 ± 0.09	this study
Ureilites	0.98 ± 0.12	0.89 ± 0.09	0.38 ± 0.04	0.21 ± 0.03	0.15 ± 0.07	this study
EET 87517 (anom. ureilite)	1.90 ± 0.35	1.62 ± 0.22	0.83 ± 0.15	0.48 ± 0.15	0.47 ± 0.22	this study
PCA 82506 (anom. ureilite)	2.04 ± 0.35	1.35 ± 0.22	0.73 ± 0.15	0.30 ± 0.15	0.40 ± 0.22	this study
Angrites	0.78 ± 0.28	0.75 ± 0.11	0.39 ± 0.06	0.26 ± 0.10	0.07 ± 0.12	this study
Aubrites	0.56 ± 0.13	0.48 ± 0.05	0.25 ± 0.06	0.19 ± 0.03	0.16 ± 0.10	this study
Mesosiderites	1.21 ± 0.14	1.04 ± 0.08	0.46 ± 0.05	0.25 ± 0.03	0.19 ± 0.04	this study
Main group pallasites	1.06 ± 0.34	0.85 ± 0.22	0.38 ± 0.14	0.16 ± 0.09	0.20 ± 0.20	37
NWA 725 (ungr.)	1.55 ± 0.68	1.20 ± 0.24	0.52 ± 0.16	0.30 ± 0.05	0.63 ± 0.30	15
NWA 1058 (ungr.)	1.61 ± 0.12	1.31 ± 0.11	0.68 ± 0.09	0.38 ± 0.10	0.40 ± 0.08	this study
IAB (MG, sL)	-0.03 ± 0.30	0.04 ± 0.10	-0.07 ± 0.05	0.00 ± 0.02	0.02 ± 0.03	11
IAB (sH)	0.96 ± 0.65	0.94 ± 0.27	0.38 ± 0.13	0.24 ± 0.02	0.24 ± 0.17	15
IC*	0.97 ± 0.68	0.88 ± 0.26	0.36 ± 0.06	0.22 ± 0.05	0.29 ± 0.11	11, 13
IIAB	1.52 ± 0.86	1.20 ± 0.22	0.55 ± 0.16	0.26 ± 0.07	0.35 ± 0.18	11
IIE	0.86 ± 0.32	0.71 ± 0.15	0.29 ± 0.13	0.12 ± 0.07	0.24 ± 0.07	14
IIIAB	1.35 ± 0.69	1.07 ± 0.24	0.44 ± 0.15	0.24 ± 0.04	0.44 ± 0.24	11
IIIE*	1.33 ± 0.15	1.01 ± 0.14	0.50 ± 0.10	0.28 ± 0.08	0.30 ± 0.11	13, 14, 37
IVA	0.99 ± 0.79	0.80 ± 0.28	0.37 ± 0.13	0.19 ± 0.06	0.24 ± 0.30	11
Gebel Kamil (ungr.)	0.31 ± 0.91	0.34 ± 0.30	0.07 ± 0.15	0.04 ± 0.08	0.32 ± 0.22	11

Mo isotope data (normalized to ^{98}Mo/^{96}Mo) and references for bulk meteorites as displayed in Fig. 1 and used for calculations of the CC- and NC-lines. *Combined mean of samples with small or no CRE effects.

References in Supplementary Information

38. Goderis, S., Brandon, A. D., Mayer, B. & Humayun, M. s-Process Os isotope enrichment in ureilites by planetary processing. *Earth Planet. Sci. Lett.* **431**, 110-118 (2015).
39. Yokoyama, T., Alexander, C. M. O. D. & Walker, R. J. Assessment of nebular versus parent body processes on presolar components present in chondrites: Evidence from osmium isotopes. *Earth Planet. Sci. Lett.* **305**, 115-123 (2011).
40. Burkhardt, C., Kleine, T., Dauphas, N. & Wieler, R. Origin of isotopic heterogeneity in the solar nebula by thermal processing and mixing of nebular dust. *Earth Planet. Sci. Lett.* **357-358**, 298-307 (2012).
41. Dauphas, N., Marty, B. & Reisberg, L. Molybdenum Nucleosynthetic Dichotomy Revealed in Primitive Meteorites. *Astrophys. J.* **569**, L139-L142 (2002).
42. Weis, D. *et al*. High-precision isotopic characterization of USGS reference materials by TIMS and MC-ICP-MS. *Geochem. Geophys. Geosyst.* **7**, Q08006 (2006).
43. Hin, R. C., Burkhardt, C., Schmidt, M. W., Bourdon, B. & Kleine, T. Experimental evidence for Mo isotope fractionation between metal and silicate liquids. *Earth Planet. Sci. Lett.* **379**, 38-48 (2013).
44. Greber, N. D., Puchtel, I. S., Nägler, T. F. & Mezger, K. Komatiites constrain molybdenum isotope composition of the Earth's mantle. *Earth Planet. Sci. Lett.* **421**, 129-138 (2015).
45. Marchi, S., Canup, R. M. & Walker, R. J. Heterogeneous delivery of silicate and metal to the Earth by large planetesimals. *Nature Geosci.* **11**, 77-81 (2018).
46. Wade, J., Wood, B. J. & Tuff, J. Metal-silicate partitioning of Mo and W at high pressures and temperatures: Evidence for late accretion of sulphur to the Earth. *Geochim. Cosmochim. Acta* **85**, 58-74 (2012).
47. Burkhardt, C., Hin, R. C., Kleine, T. & Bourdon, B. Evidence for Mo isotope fractionation in the solar nebula and during planetary differentiation. *Earth Planet. Sci. Lett.* **391**, 201-211 (2014).
48. Hilton, C. D., Bermingham, K. R., Walker, R. J. & McCoy, T. J. Genetics, crystallization sequence, and age of the South Byron Trio iron meteorites: New insights to carbonaceous chondrite (CC) type parent bodies. *Geochim. Cosmochim. Acta* **251**, 217-228 (2019).
49. Dauphas, N., Marty, B. & Reisberg, L. Molybdenum Evidence for Inherited Planetary Scale Isotope Heterogeneity of the Protosolar Nebula. *Astrophys. J.* **565**, 640-644 (2002).
50. Render, J., Fischer-Gödde, M., Burkhardt, C. & Kleine, T. The cosmic molybdenum-neodymium isotope correlation and the building material of the Earth. *Geochem. Persp. Let.* **3**, 170-178 (2017).

Supplementary Data 1
Data file for Supplementary Table 4. Summary of Mo isotope data and references for bulk meteorites as displayed in Fig. 1 and used for calculations of CC- and NC-lines.